

Collective anisotropic flow in small and large systems

Niseem Magdy,^{1,*} Peifeng Liu,¹ and Roy A. Lacey^{1,†}

¹*State University of New York (Stony Brook)*

Abstract

The flow harmonics v_1^{even} , v_2 and v_3 , are extracted and studied as a function of transverse momentum (p_T) and mean charge particle multiplicity $\langle N_{\text{ch}} \rangle$, in U+U ($\sqrt{s_{NN}} = 193$ GeV), Au+Au, Cu+Au, Cu+Cu, d+Au and p+Au collisions at $\sqrt{s_{NN}} = 200$ GeV. The measurements validate the expected influence of initial-state eccentricity, system size and specific shear viscosity (η/s) on the magnitude of the flow harmonics, consistent with hydrodynamic-like viscous attenuation in the medium produced in these collisions. The measurements and their scaling properties, indicate similar final-state collective effects with comparable η/s values for the hot and dense matter created in all of the systems studied.

* Niseem.Abdelrahman@stonybrook.edu

† Roy.Lacey@stonybrook.edu

CONTENTS

I. Data, Event and Track selection	2
A. $p + Au$ QA	3
II. Correlation function technique	8
A. v_n for $n > 1$ and short rang non-flow subtraction	8
B. Dipolar flow (v_1^{even}) and long rang non-flow subtraction	15
1. Extraction of dipolar flow (v_1^{even})	17
III. Systematic uncertainty estimates	21
1. Systematic uncertainty from fitting procedure	21
IV. Results	23
A. Comparisons	28
B. Multi-particle correlation	30
C. The ϵ_2 used in this work	31
References	31

I. DATA, EVENT AND TRACK SELECTION

The data and the associated cuts (vertex cut, trigger-ID, nHitMin, DCA, p_T , η , etc) used in the analysis are summarized in Tables I and I. Tables I summarizes the Trigger, Production, Trigger ID and and vertex cut respectively. The centrality selections are based on StRefMultCorr Class from:*offline/users/hmasui/StRefMultCorr*. The track cuts are summarized in Table I. The selections and cuts outlined in Tables I and I were used in concert with Eq. 1 to generate correlation functions. In turn, these correlation functions are used to obtain v_n , c.f., Eqs. 2 and 3.

Trigger Name	Production	Vertex Cut	Trigger ID
<i>production_pAu200₂015</i>	<i>P16id</i>	$ V_z < 30cm$	500904
<i>dAuMinBias</i>	<i>P08ie</i>	$ V_z < 50cm$	210000
			210020
<i>cuProductionMinBias</i>	<i>P06ib</i>	$ V_z < 40cm$	66007
	<i>P07ic</i>		
<i>cuAu_pproduction₂012</i>	<i>P14ia</i>	$ V_z < 40cm$	410005
			410008
<i>UU_pproduction₂012</i>	<i>P12id</i>	$ V_z < 40cm$	400005
			400015
			400025
			400035
<i>AuAu200 – Production</i>	2004	$ V_z < 30cm$	15007

<i>Cut</i>	<i>TPC – tracks</i>
<i>DCA cm</i>	< 3
<i>p_T GeV/c</i>	> 0.2
$ \eta \text{ cm}$	< 1
<i>nHitMin</i>	> 10
V_r	< 2

Tab. I. The track cut that we used in our calculations .

A. $p + Au$ QA

In this subsection we shows the $p + Au$ QA plots like RefMult, V_z , p_T , η , ϕ and DCA before and after the cuts.

- Trigger ID 500904
- Bad Run list

16149004, 16129001, 16131026, 16133014, 16134012, 16138053, 16143022,
, 16154010, 16154021, 16155017, 16155039, 16156010, 16156028, 16156030
, 16156031, 16156032, 16156033, 16156034, 16158021, 16158039, 16159019

- Event cuts

$$|V_z| < 30, |V_x| < 1, |V_y| < 1 \text{ and } nTofHits < 2$$

- Track cuts $DCA < 1, 0.2 < p_T < 4, |\eta| < 1$ and $nHitMin > 15$

- QA plots Here we present Fig.(1,2,3,4,5,6 and 7).

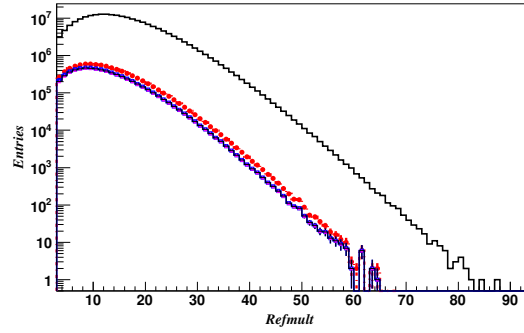


Fig. 1. Black line represent *refmult* without any cut, red points represent *refmult* after removing the bad run list, blue points represent *refmult* after event cuts.

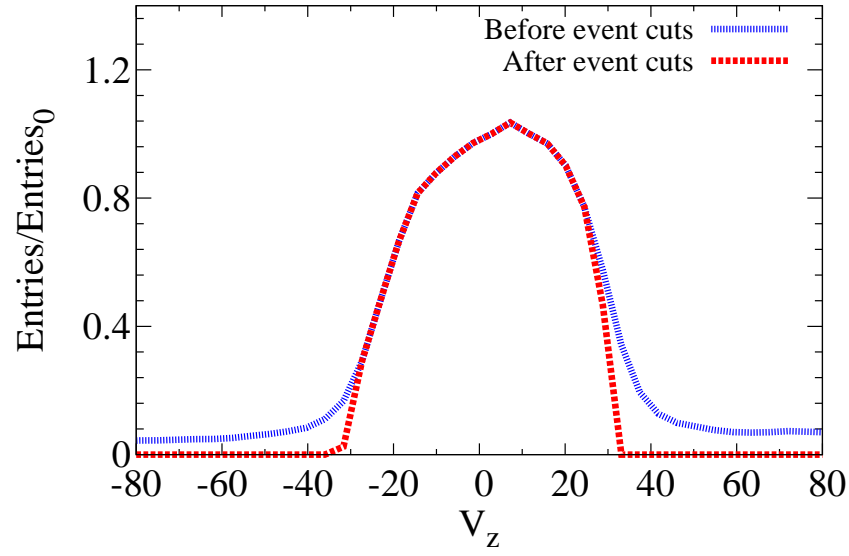


Fig. 2. Right had panel represent V_z without any cut, mid-panel represent V_z after removing the bad run list, left-panel represent V_z after event cuts.

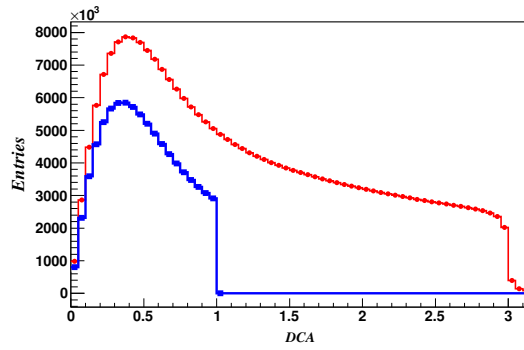


Fig. 3. Red line represent DCA without any cut and blue points represent DCA after track cuts.

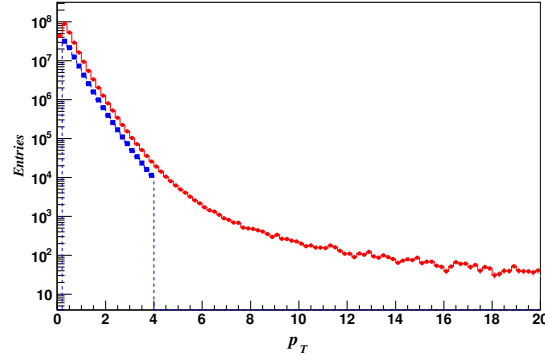


Fig. 4. Red line represent p_T without any cut and blue points represent p_T after track cuts.

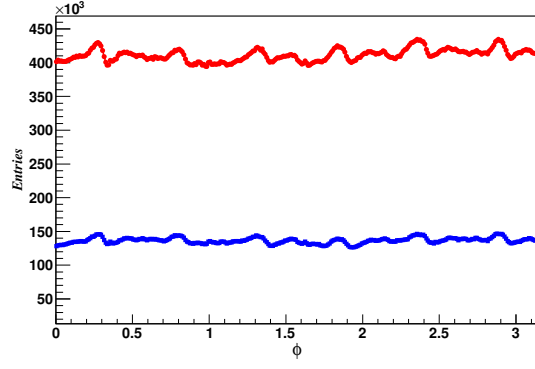


Fig. 5. Red line represent ϕ without any cut and blue points represent ϕ after track cuts.

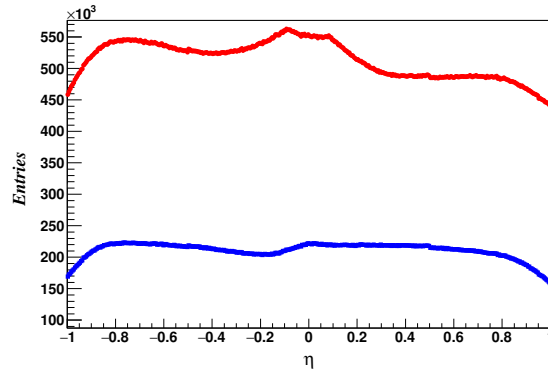


Fig. 6. Red line represent η without any cut and blue points represent η after track cuts.

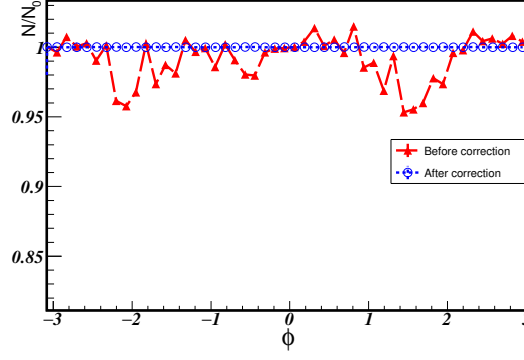


Fig. 7. ϕ distribution before and after the acceptance correction.

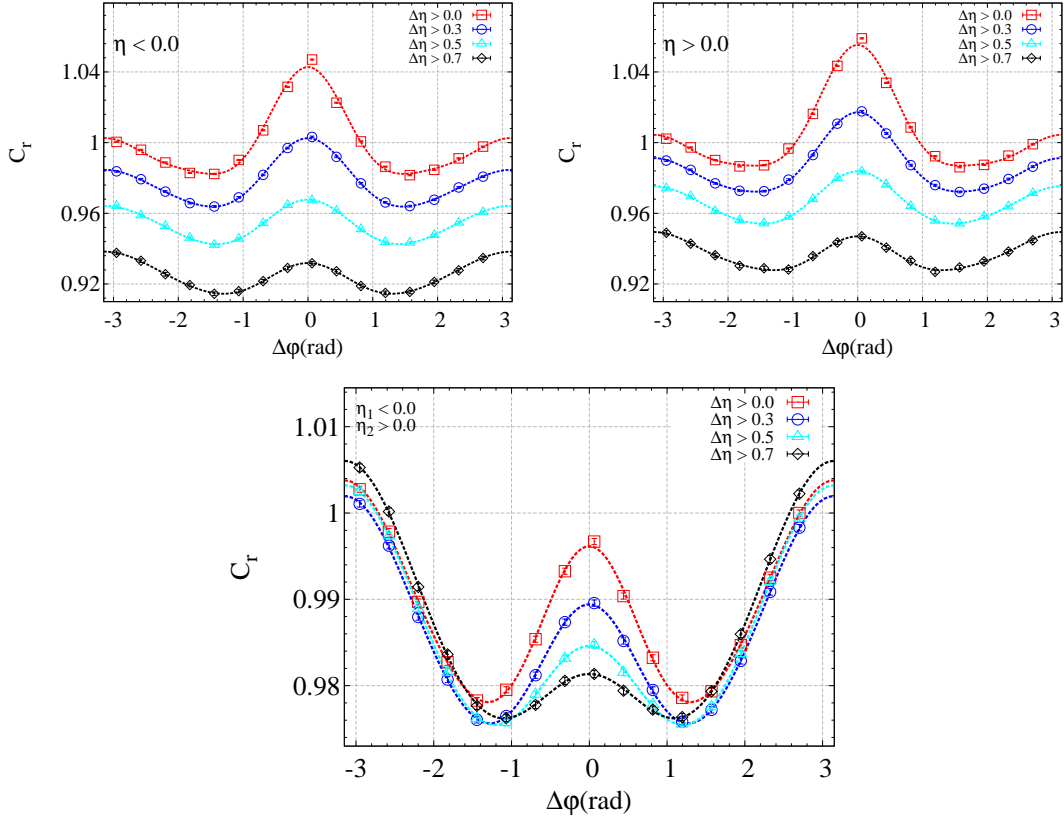


Fig. 8. Correlation function for $p + Au$ collisions at $\sqrt{s_{NN}} = 200$ GeV for $\eta_1 < 0$ and $\eta_2 < 0$ (left panel), $\eta_1 > 0$ and $\eta_2 > 0$ (right panel) and $\eta_1 > 0$ and $\eta_2 < 0$ (bottom panel).

II. CORRELATION FUNCTION TECHNIQUE

A. v_n for $n > 1$ and short rang non-flow subtraction

All techniques used to extract v_n are related to the correlation function. The correlation function carry flow and non-flow(HBT, Resonance decay and Jet like correlation) signals as well as some residual detector effects(track merging/splitting). The two particle azimuthal correlation function $C(\Delta\phi, \Delta\eta)$ can be expressed as,

$$C(\Delta\phi, \Delta\eta) = \frac{(dN/d\Delta\phi)_{Same}}{(dN/d\Delta\phi)_{Mix}} \quad (1)$$

where $(dN/d\Delta\phi)_{Same}$ is the distribution of charged hadron pairs from the *same* event and $(dN/d\Delta\phi)_{Mix}$ is the pair distribution for particles from different events, belonging to the same class; $\Delta\phi$ is the azimuthal angle difference for particle pairs. Event classes, which retain the residual detector single particle relative efficiencies etc., eliminate the the genuine two-particle physics correlations. To optimize mixing, events are pooled into classes to ensure similar global characteristics for same-event and mixed-event tracks. Twenty Vz classes and 10 centrality classes were used. A pool depth of 10 was employed for mixing.

The Fourier coefficients v_{nn} , used to characterize the magnitude of the azimuthal anisotropy, are obtained from the correlation function as,

$$v_{nn} = \frac{\sum_{\Delta\phi} C(\Delta\phi, \Delta\eta) \cos(n\Delta\phi)}{\sum_{\Delta\phi} C(\Delta\phi, \Delta\eta)}, \quad (2)$$

where $C(\Delta\phi, \Delta\eta) = \frac{(dN/d\Delta\phi)_{Same}}{(dN/d\Delta\phi)_{Mix}}$. For flow dominated correlations, the Fourier coefficient v_{nn} factorizes into the product of two single-particle distributions:

$$v_{nn}(p_T^t, p_T^a) = v_n(p_T^t) v_n(p_T^a), \quad (3)$$

where the superscripts t and a refer to trigger and associated particles respectively. For a fixed- p_T selection

$$v_n^2 = \frac{\sum_{\Delta\phi} C(\Delta\phi, \Delta\eta) \cos(n\Delta\phi)}{\sum_{\Delta\phi} C(\Delta\phi, \Delta\eta)}. \quad (4)$$

Representative examples of the correlation functions obtained in this analysis are shown in Figs. 9, 10 and 11, 12 and 13 for several centrality selections and beam energies. These

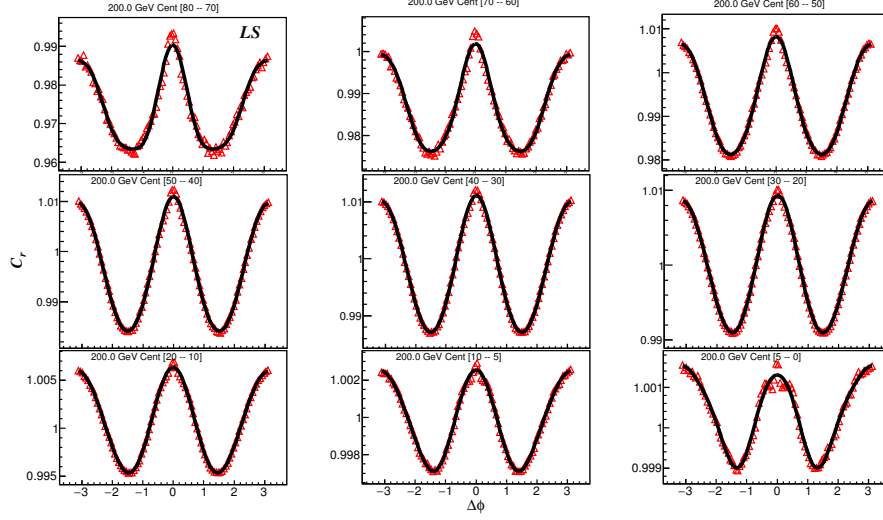


Fig. 9. Like sign (LS) p_T -integrated correlation function for Au+Au collisions at $\sqrt{s_{NN}} = 200$ GeV. The correlation functions are generated without a $\Delta\eta$ cut.

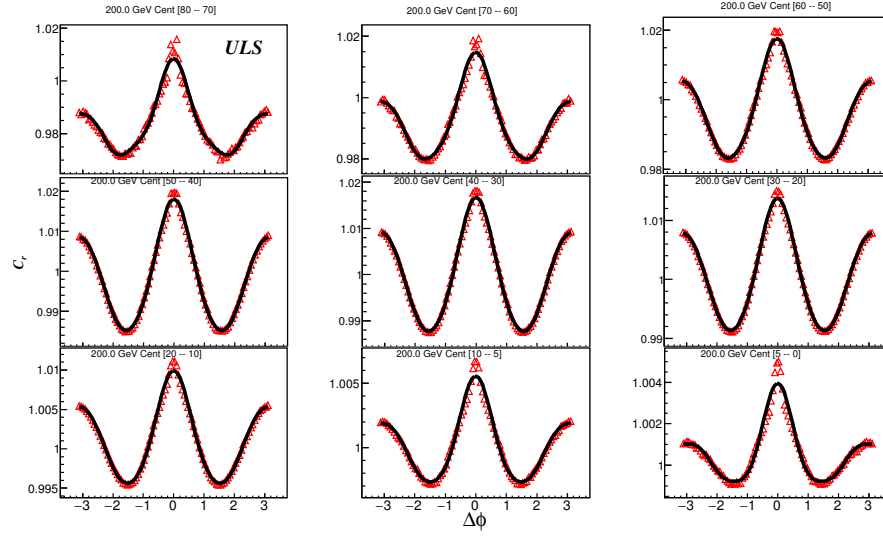


Fig. 10. Unlike sign (ULS) p_T -integrated correlation functions for Au+Au collisions at $\sqrt{s_{NN}} = 200$ GeV for several centrality selections. The correlation functions are generated without a $\Delta\eta$ cut.

correlation functions reflect both flow and non-flow contributions, as well as some residual detector/tracking effects. The latter effects are especially evident in the top left panels of Figs. 9 and 10. We attribute the dip (peak) to track merging (splitting) effects. A small cut over $|\Delta\eta|$ could fix this effect as in Figs. 11 and 12. The short-range non-flow contributions

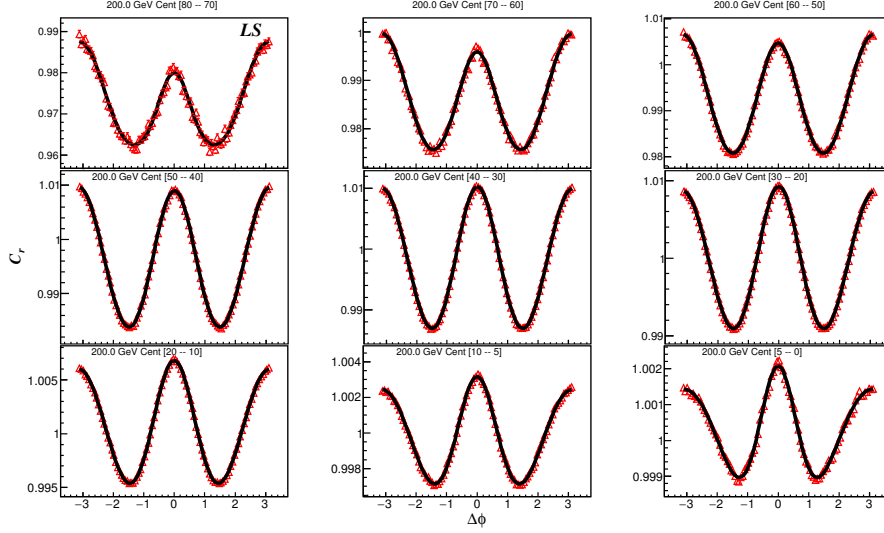


Fig. 11. Like sign (LS) p_T -integrated correlation function for Au+Au collisions at $\sqrt{s_{NN}} = 200$ GeV. The correlation functions are generated without a $\Delta\eta > 0.3$ cut.

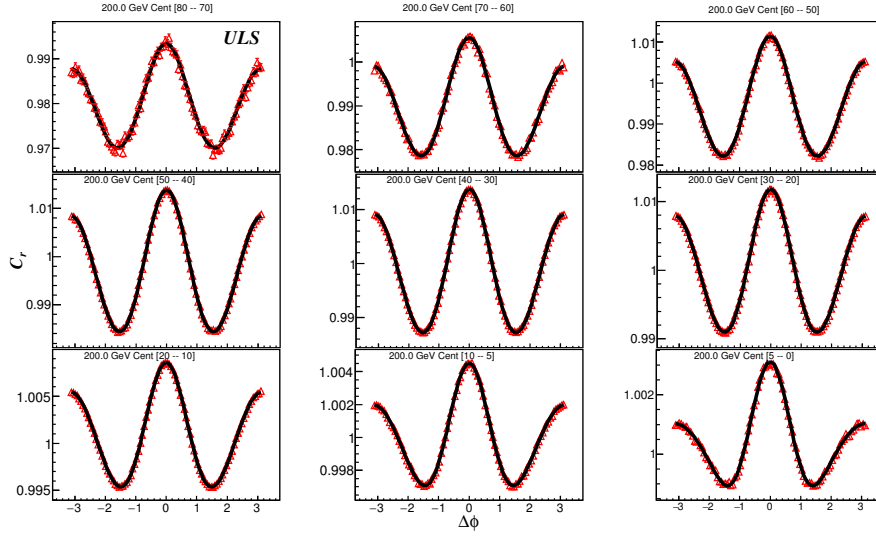


Fig. 12. Unlike sign (ULS) p_T -integrated correlation functions for Au+Au collisions at $\sqrt{s_{NN}} = 200$ GeV for several centrality selections. The correlation functions are generated without a $\Delta\eta > 0.3$ cut.

(HBT, Resonance decay and Jet-like correlations) and the residual detector effects (track merging/splitting) dominate at small $\Delta\eta$. Consequently, we explored the utility of a $|\Delta\eta|$ cut to suppress these effects.

The correlation functions shown in Figs. 9 and 10 were generated for the full $\Delta\eta$ range

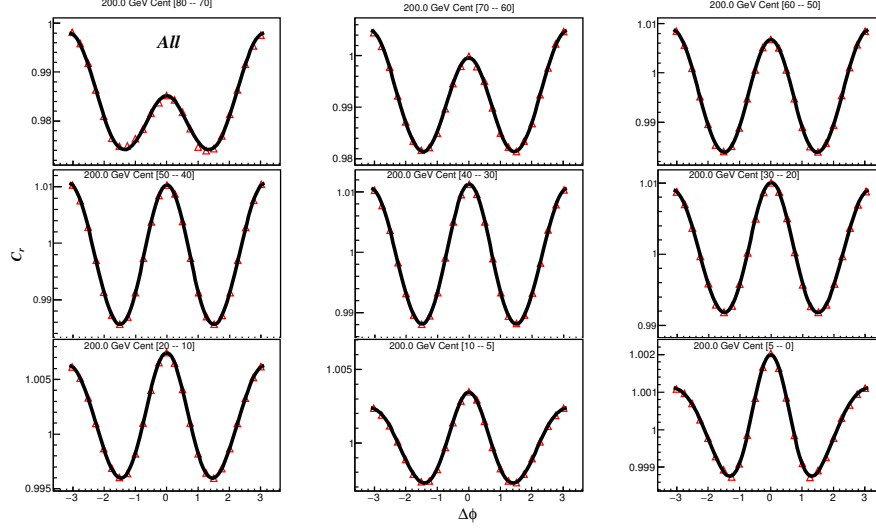


Fig. 13. All charged particles p_T -integrated correlation functions for Au+Au collisions at $\sqrt{s_{NN}} = 200$ GeV for several centrality selections. The correlation functions are generated without a $|\Delta\eta| > 0.7$ cut.

for both like sign (LS) and unlike sign (ULS) charged hadrons. They indicate that the distortions which result from non-flow contributions and detector effects, persist over the full range of centralities. Similar results were obtained for other beam energies. To suppress these distortions, the correlation functions were studied as a function of $|\Delta\eta|$ cut, for several p_T and centrality selections, over the full span of beam energies. This comprehensive study indicated that the cut $|\Delta\eta| > 0.7$, leads to significant suppression of track merging/splitting and non-flow contributions, while allowing reasonable statistical significance for our study over the full beam energy range. Here, it is noteworthy that a large $|\Delta\eta|$ leads to a significant reduction in the available statistics, especially for the lower beam energies Fig. 13.

The representative set of correlation functions shown in Figs. 14, 15 and 16, clearly indicates that the "distortions" [due to detector effects and non-flow] evident in Figs. 9 and 10 are suppressed by the $|\Delta\eta| > 0.7$ cut.

The comparisons shown in Fig. 17 for LS- and ULS- v_2 for $|\Delta\eta| > 0.7$, confirming the utility of this cut for suppressing non-flow contributions. Consequently, the cut $|\Delta\eta| > 0.7$, was employed to suppress short-range non-flow contributions for all systems studied. More information could be found in the v1 and vn analysts notes[—].

Also another comparison between our measurement and different collaborators measure-

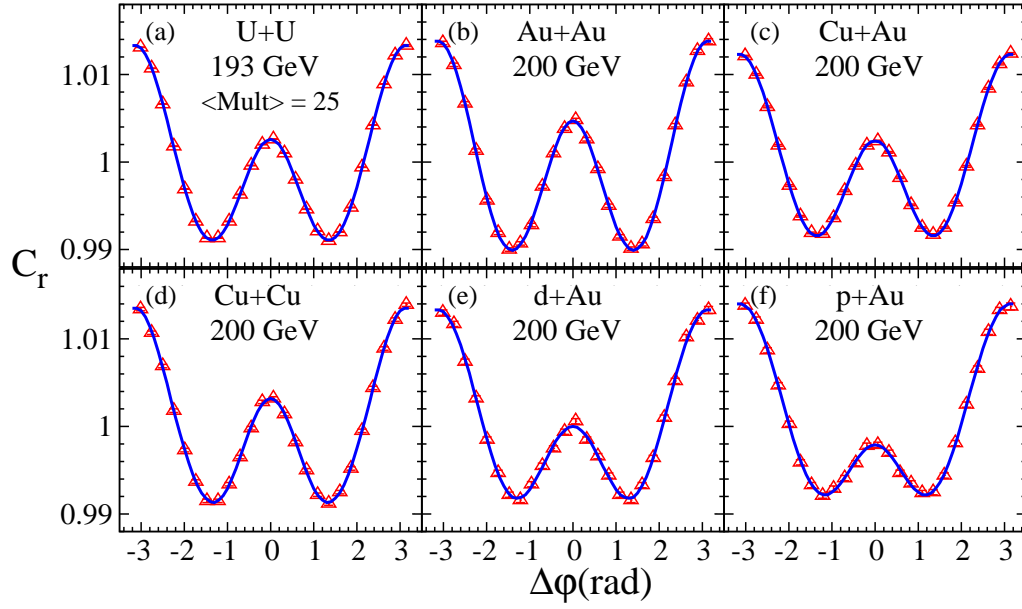


Fig. 14. p_T -integrated correlation functions for different collision systems for $\langle Mult \rangle = 25$ as indicated; the correlation functions are generated for $|\Delta\eta| > 0.7$.

ments could be found in [appendix A](#).

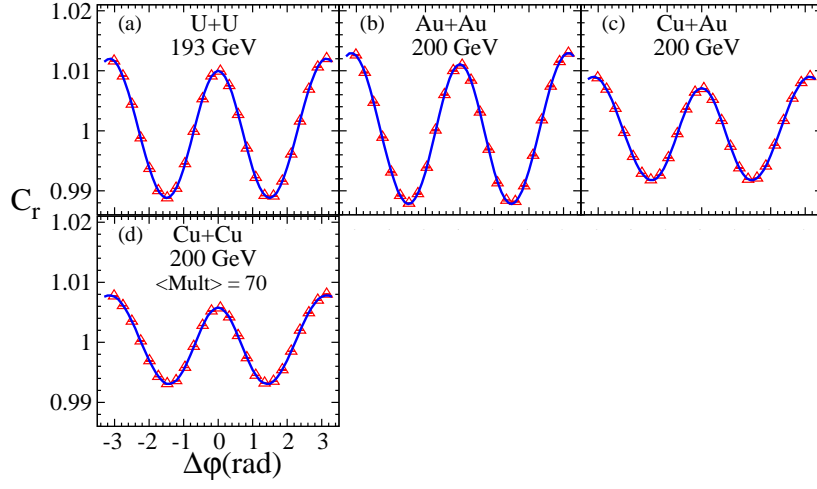


Fig. 15. p_T -integrated correlation functions for different collision systems for $\langle Mult \rangle = 70$ as indicated; the correlation functions are generated for $|\Delta\eta| > 0.7$.

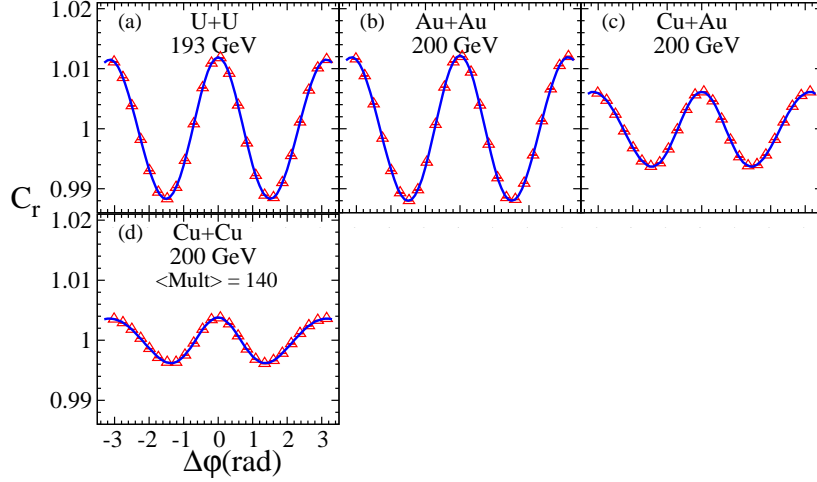


Fig. 16. p_T -integrated correlation functions for different collision systems for $\langle Mult \rangle = 140$ as indicated; the correlation functions are generated for $|\Delta\eta| > 0.7$.

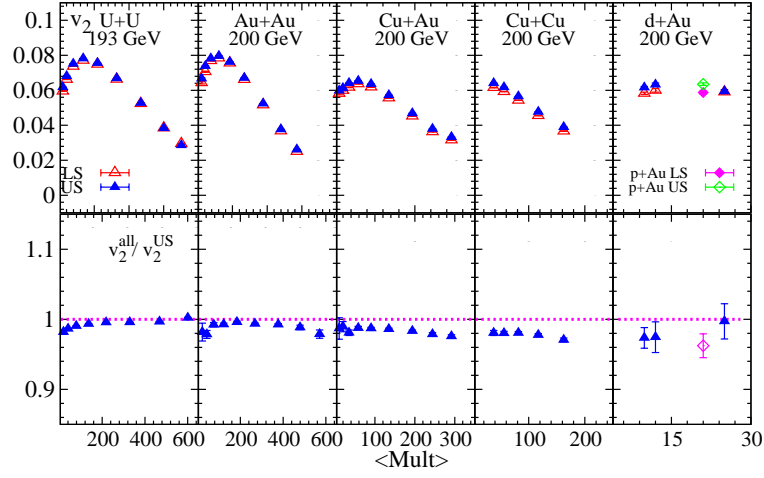


Fig. 17. Comparison of LS- and ULS- v_2 for all systems collisions at $\sqrt{s_{NN}} \sim 200$ GeV for $|\Delta\eta| > 0.7$.

B. Dipolar flow (v_1^{even}) and long rang non-flow subtraction

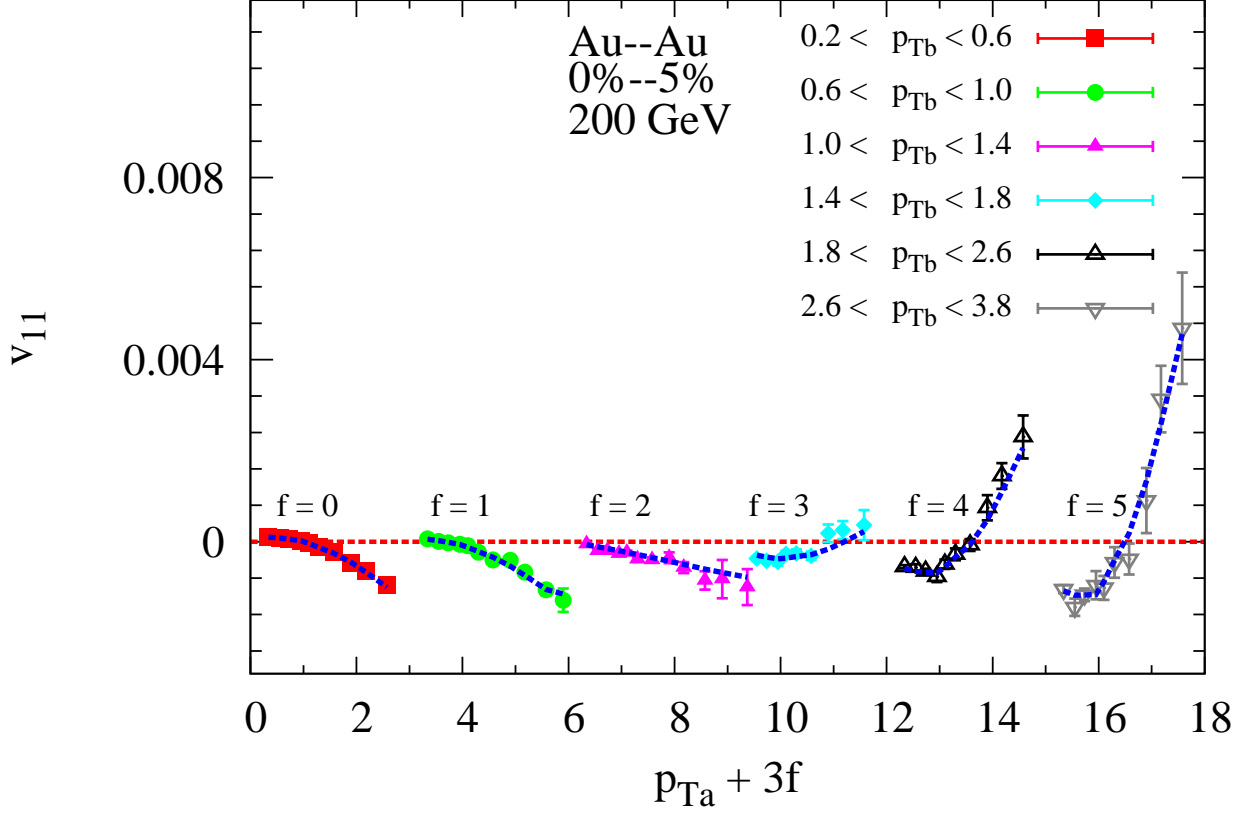


Fig. 18. Illustration of the simultaneous fit of $v_{1,1}$ Au+Au data ($\sqrt{s_{NN}} = 200$ GeV) with Eq. 7.

As discussed earlier, the two particle Fourier coefficient v_{nn} are obtained from the correlation function Figs.(14, 15 and 16) as,

$$v_{nn} = \frac{\sum_{\Delta\phi} C(\Delta\phi, \Delta\eta) \cos(n\Delta\phi)}{\sum_{\Delta\phi} C(\Delta\phi, \Delta\eta)}, \quad (5)$$

where $C(\Delta\phi, \Delta\eta) = \frac{(dN/d\Delta\phi)_{\text{Same}}}{(dN/d\Delta\phi)_{\text{Mix}}}$. The Fourier coefficients v_{nn} factorizes into the product of two single-particle distributions for $n > 1$ see Figs.(19, 20 and 21):

$$v_{nn}(p_T^t, p_T^a) = v_n(p_T^t) v_n(p_T^a), \quad (6)$$

where the superscripts t and a refer to trigger and associated particles that can be taken from different p_T bins. Several studies (including this work) have shown that, while this

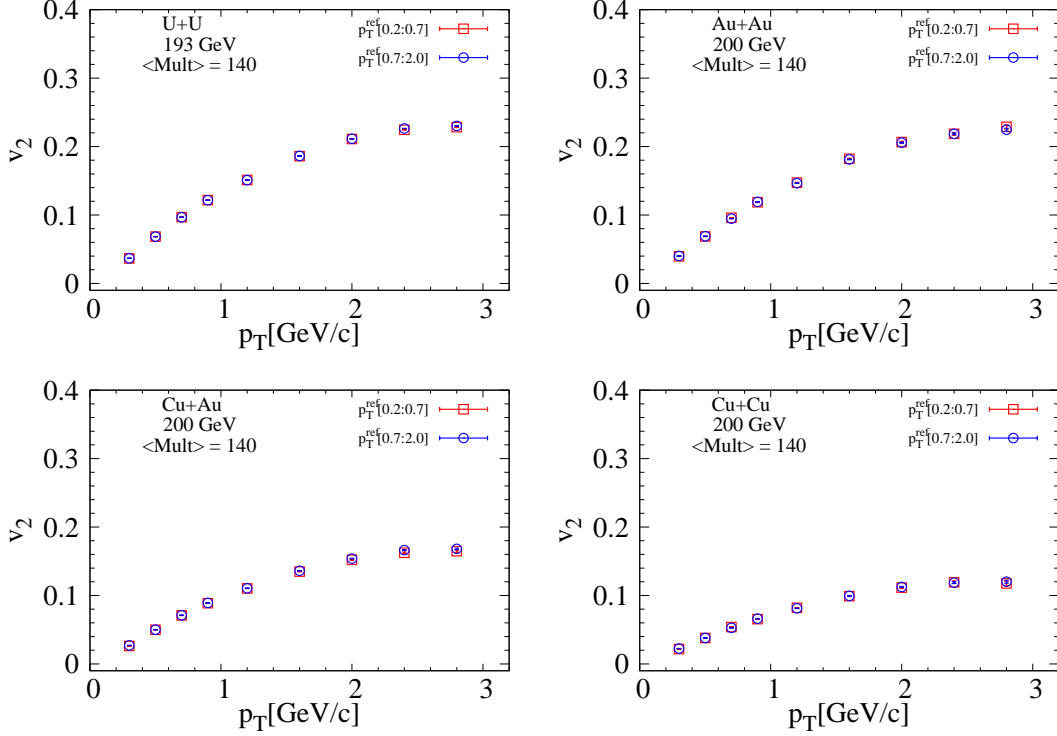


Fig. 19. v_2 vs p_T for different systems at two different p_T^{ref} and $\langle Mult \rangle = 140$.

factorization holds reasonably well for $n > 1$ evaluated with a sizable $\Delta\eta$ gap Figs.(19, 20 and 21), it breaks down for $n = 1$.

This break down is to be expected for v_1 due to the strong influence of long-range correlations induced by global momentum conservation. Since such correlations add to the flow correlations of interest, it is necessary to subtract them;

$$v_{1,1}(p_T^t, p_T^a) = v_n(p_T^t) v_n(p_T^a) - \frac{p_T^t p_T^a}{M \langle p_T^2 \rangle}, \quad (7)$$

where M and $\langle p_T^2 \rangle$ are the multiplicity and average squared transverse momentum for the events, respectively. The v_1 can be separated into a rapidity-odd component and a rapidity-even component. The rapidity-odd v_1 stems from the deflection of the colliding ions, and hence, changes sign from negative η to positive η . The rapidity-even v_1 is argued to be related to the dipole anisotropy of the pressure gradient arising from the dipole asymmetry of the nuclear overlap; this dipole asymmetry is mainly due to fluctuations in the initial-state geometry.

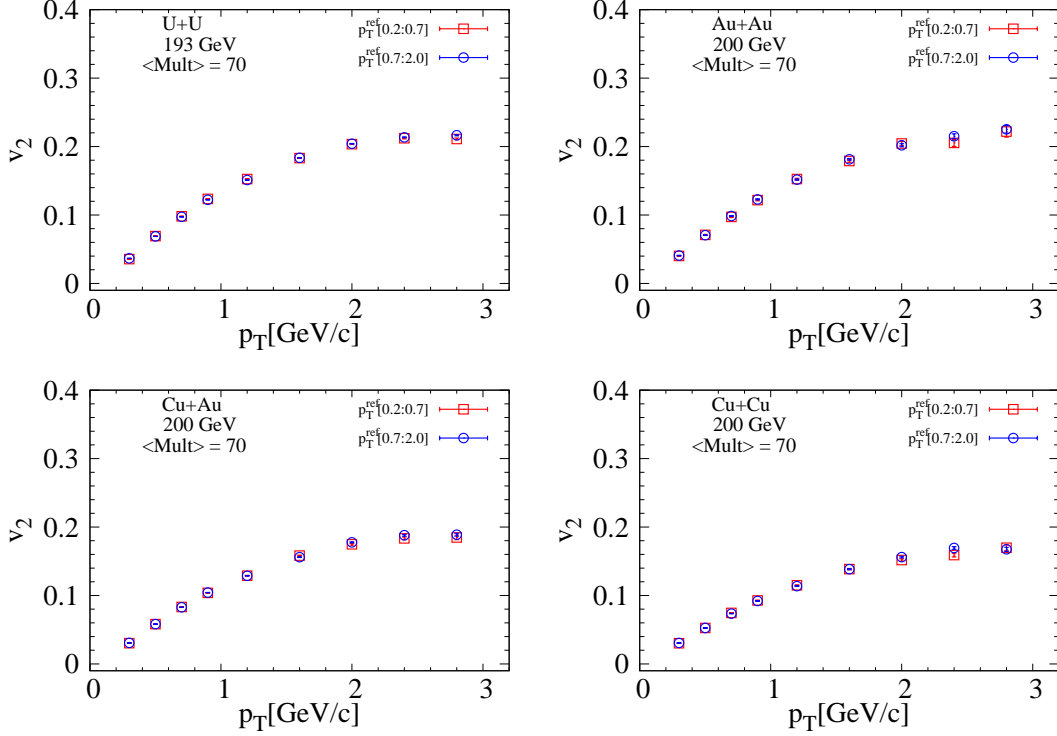


Fig. 20. v_2 vs p_T for different systems at two different p_T^{ref} and $\langle Mult \rangle = 70$.

1. Extraction of dipolar flow (v_1^{even})

For a given centrality selection, the left hand side of Eq. 7 represents the $N \times N$ matrix which we fit with the right hand side using $N + 1$ parameters; N values of $v_1^{even}(p_T)$ and one additional parameter C , the coefficient of momentum conservation. Fig. 18 illustrates the efficacy of the fitting procedure for central Au+Au collisions at $\sqrt{s_{NN}} = 200$ GeV. The curves in each figure (obtained with Eq. 7) illustrates the effectiveness of the simultaneous fits, as well as the constraining power of the data. That is, $v_{11}(p_T^t)$ evolves from negative to positive values as the selection range for p_T^a is increased. more information are in v1 analyses note[—]

Figure 22 shows a representative set of the $v_1^{even}(p_T)$ values obtained for the beam energies indicated. In contrast to the rapidity-odd directed flow, these flow values indicate the characteristic pattern of a change from negative $v_1^{even}(p_T)$ at low- p_T , to positive $v_1^{even}(p_T)$ for $p_T \gtrsim 1$ GeV, with a crossing point that shifts with $\sqrt{s_{NN}}$. This predicted pattern for rapidity-even dipolar flow stems from the requirement that the net transverse momentum of the system is zero, *i.e.*, $\langle p_T v_1^{even}(p_T) \rangle = 0$, which implies that the flow direction of low-

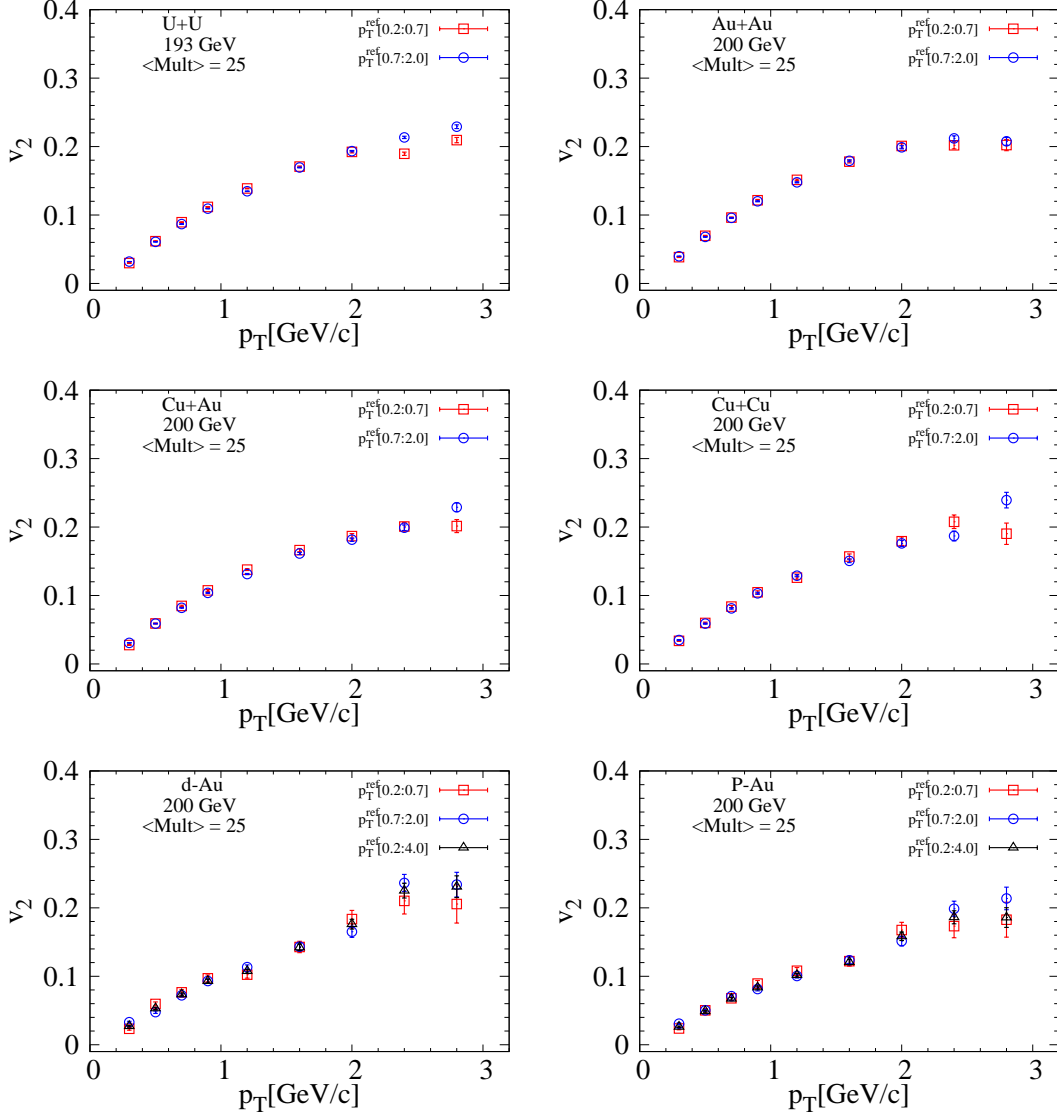


Fig. 21. v_2 vs p_T for different systems at two different p_T^{ref} and $\langle Mult \rangle = 25$.

p_T particles is opposite to that for high- p_T particles. This requirement was imposed for extraction of the $v_1^{even}(p_T)$ values.

Figure 22 shows a representative set of the $v_1^{even}(p_T)$ values obtained for the beam energies indicated. In contrast to the rapidity-odd directed flow, these flow values indicate the characteristic pattern of a change from negative $v_1^{even}(p_T)$ at low- p_T , to positive $v_1^{even}(p_T)$.

Figure.(23, ??) we shows the extracted v_1 vs. p_T^t for different systems. Our study indicates that the extracted v_1 shows no sensitivity for sign selections. Also in Fig.(25) we shows Extracted $Cu + Au$ v_1 vs. p_T^t for different $|\Delta\eta|$ selections at two different centrality selections which also indicating no sensitivity for $|\Delta\eta|$ selections.

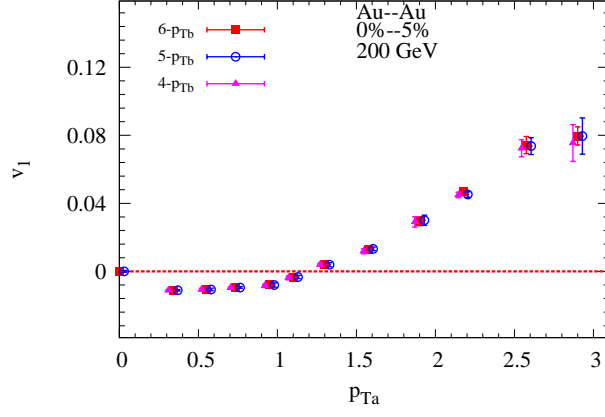


Fig. 22. Extracted v_1 vs. p_T^t for several p_T^a selections.

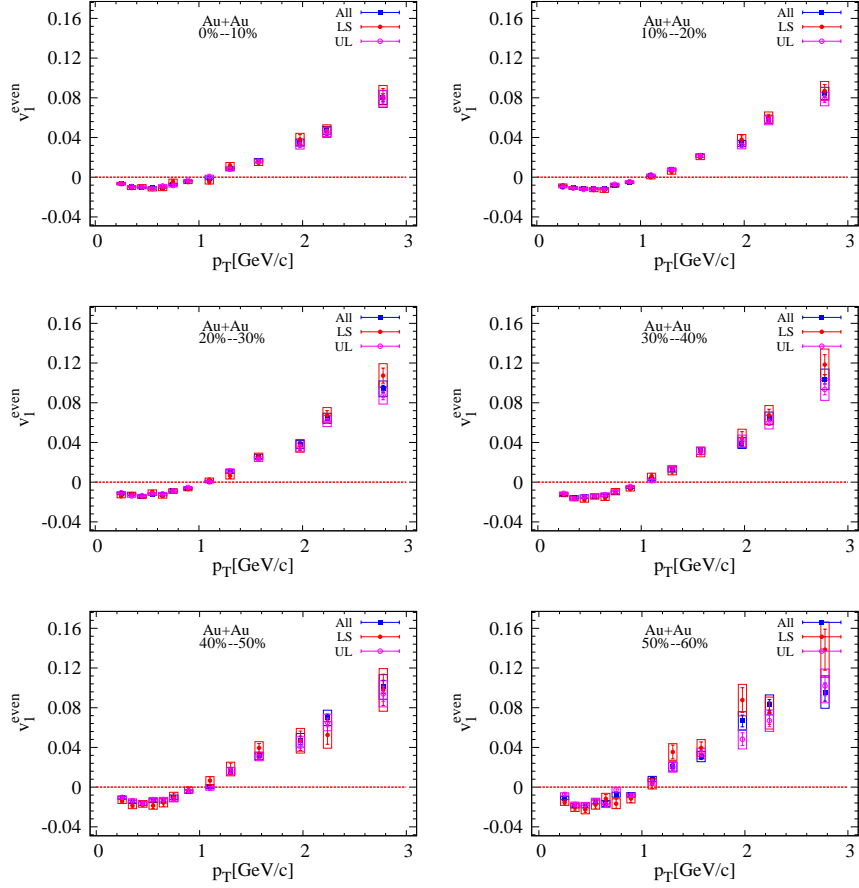


Fig. 23. Extracted v_1 vs. p_T^t for sign selections at different centralities.

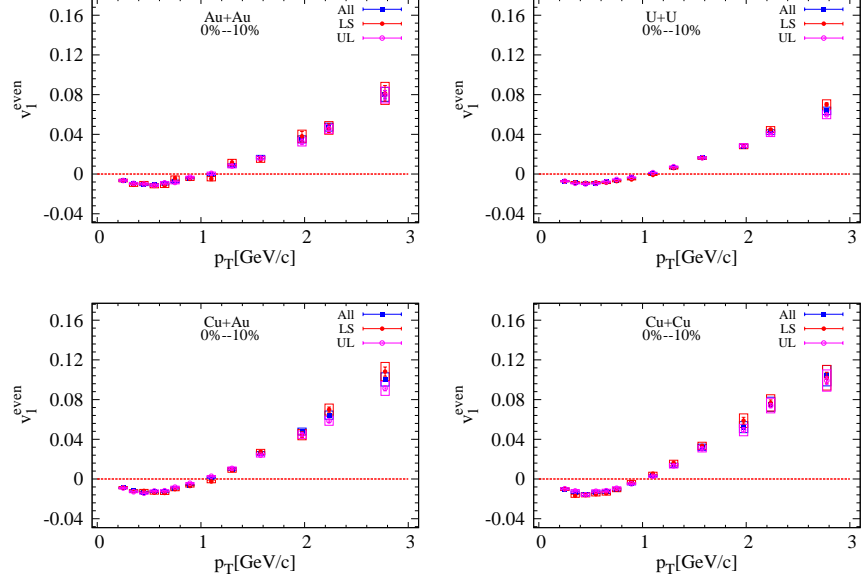


Fig. 24. Extracted v_1 vs. p_T^t for sign selections at one centrality and for different systems.

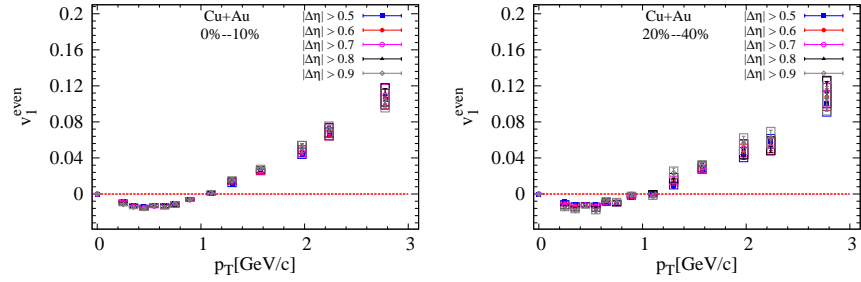


Fig. 25. Extracted $Cu + Au$ v_1 vs. p_T^t for different $|\Delta\eta|$ selections at two different centrality selections.

III. SYSTEMATIC UNCERTAINTY ESTIMATES

Systematic uncertainty estimates were obtained by;

- varying the DCA cut within a reasonable range (from 3 to 2 cm),
- comparing events with different z-vertex positions,
- comparing the results for different fit parameters,
- systematic variation of p_T^t ,
- etc.

Here, we focus on the checks related to the fitting procedure. For systematic uncertainty estimates, we use the largest and smallest deviations from our study to assign the upper and lower edge of the systematic error bands. It is noteworthy that a similar approach was employed in earlier work summarized in our “Viscous Damping of Anisotropic Flow” analysis note.

1. *Systematic uncertainty from fitting procedure*

Figure 18 show $v_{1,1}(p_T^t, p_T^a)$ for $Au + Au \sqrt{s_{NN}} = 200$. The blue dashed lines represent the results of the simultaneous fit. To estimate the systematic uncertainty associated with the fits, we vary the number of p_T^a selections used in the fit to test the fit stability. For one system as example, $v_{1,1}(p_T^t, p_T^a)$ is shown for 6, 5 and 4 p_T^a selections respectively. The extracted $v_1(p_T^t)$ show relatively small differences with the number of p_T^a values used in the fits, as indicated in Fig. 22.

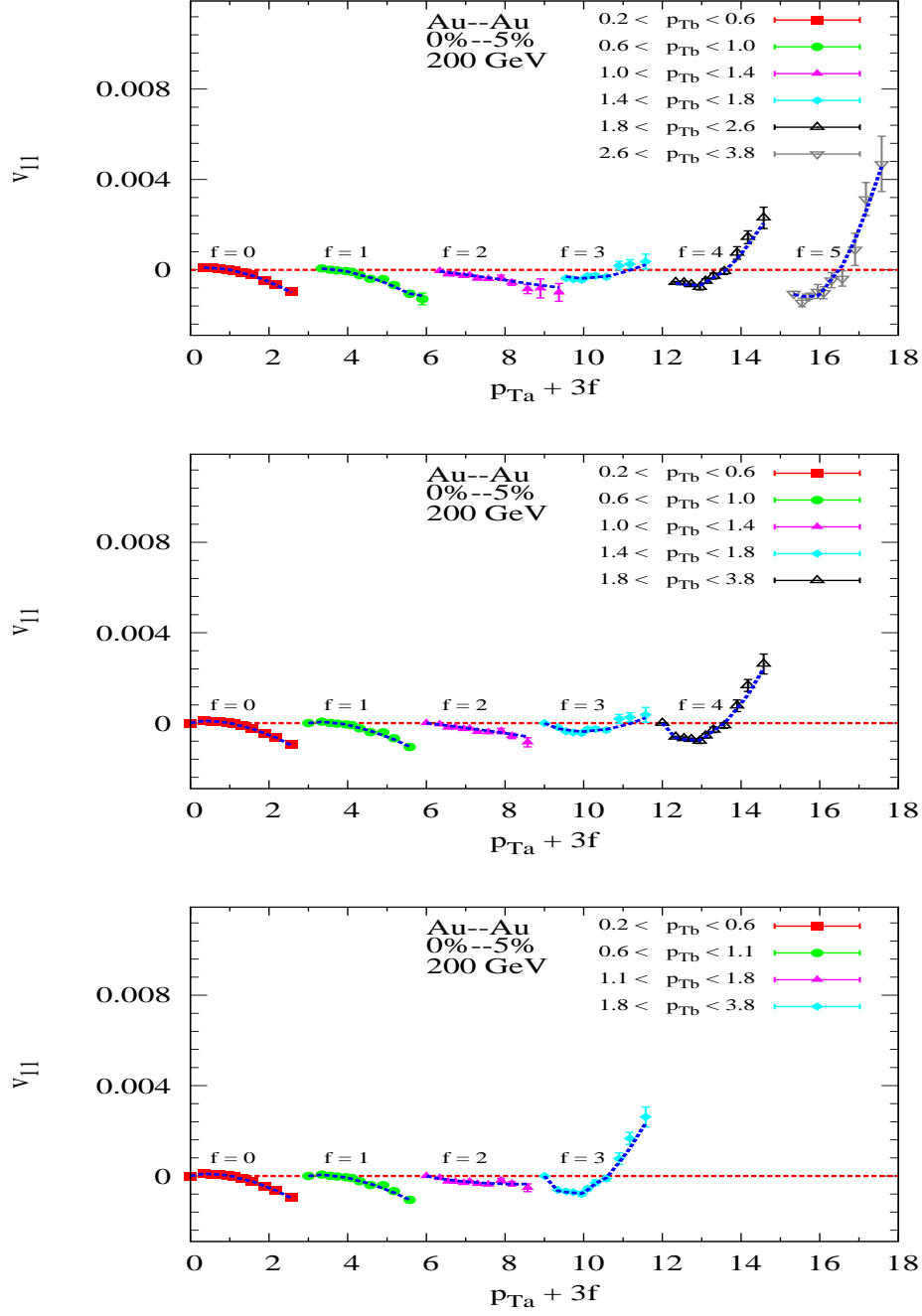


Fig. 26. Illustration of the simultaneous fit of $v_{1,1}$ Au+Au data ($\sqrt{s_{NN}} = 200$ GeV) for different p_T^a with Eq. 7.

IV. RESULTS

The proposed figures for the manuscript are Figs.27, 28, 29 and 33. Also the multi-particle cumulant method which an important toll to study the nature of the azimuthal correlations observed in heavy-ion collisions which described in appendix.

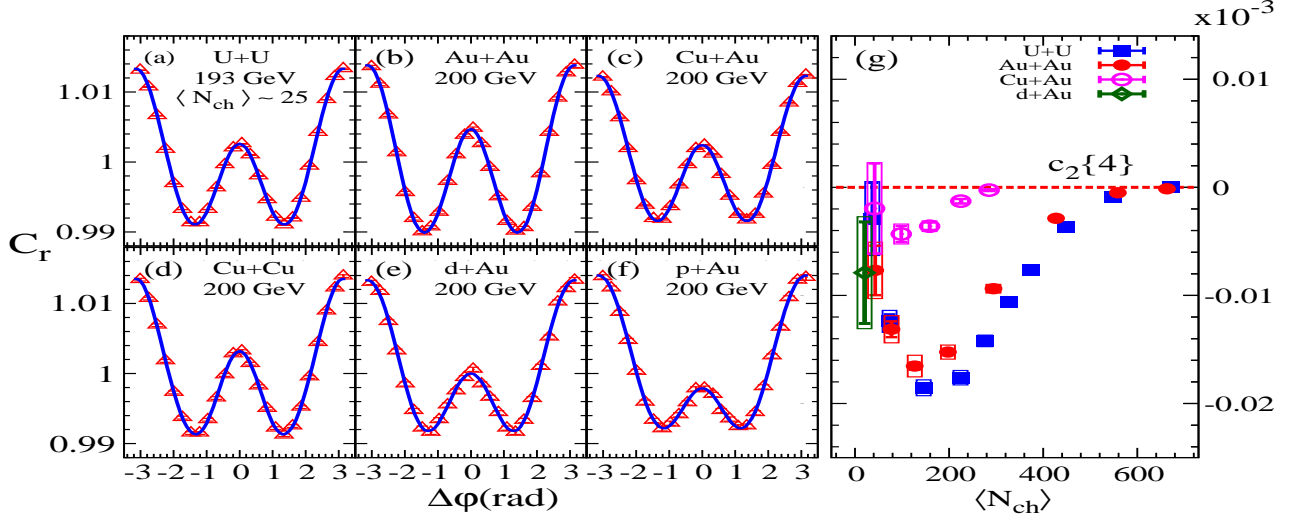


Fig. 27. Two- and multi-particle correlation functions for p_T -integrated track pairs with $|\Delta\eta| > 0.7$. Results are shown for U+U (a) collisions ($\sqrt{s_{NN}} = 193$ GeV) and Au+Au (b), Cu+Au (c), Cu+Cu (d), d+Au (e) and p+Au (f) collisions ($\sqrt{s_{NN}} = 200$ GeV) for $\langle N_{ch} \rangle = 25$. The solid curves, which show the result of a Fourier fit to the data, are drawn to guide the eye. Panel (g) shows the second-order cumulant $c_2\{4\}$ vs. $\langle N_{ch} \rangle$, obtained from the same data sets for the systems indicated.

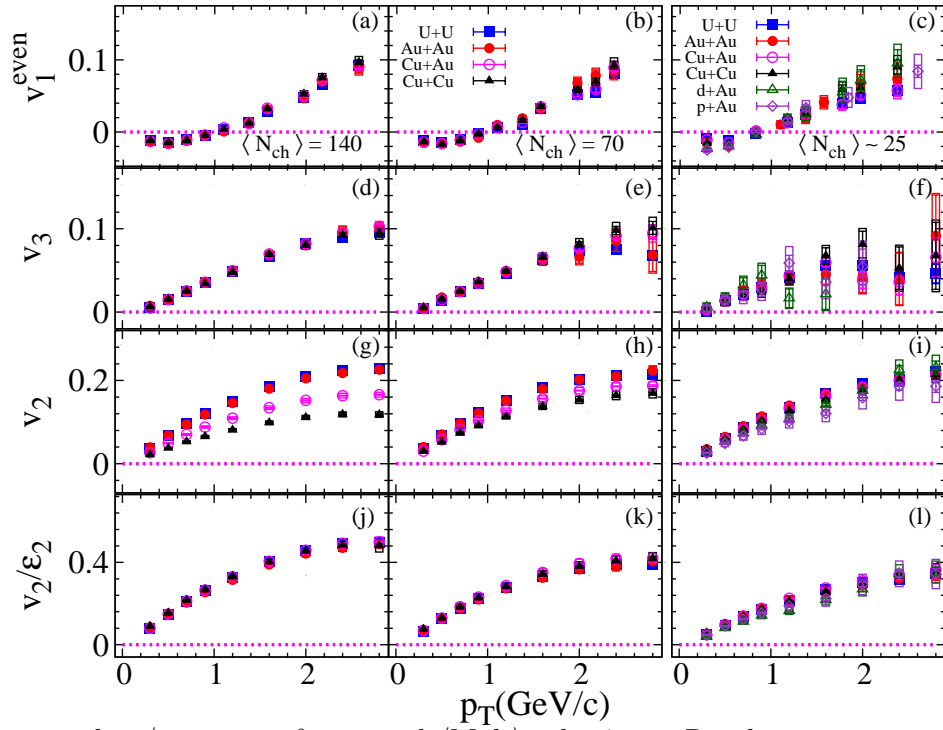


Fig. 28. $v_{1,2,3}$ and v_2/ϵ_2 vs. p_T for several $\langle \text{Mult} \rangle$ selections. Results are compared for U+U, Au+Au, Cu+Au and Cu+Cu for $\langle N_{Ch} \rangle = 140$ [(a), (d), (g), and (j)] and $\langle N_{Ch} \rangle = 70$ [(b), (e), (h), and (k)] and for U+U, Au+Au, Cu+Au, Cu+Cu, d+Au and p+Au for $\langle N_{Ch} \rangle = 25$ [(c), (f), (i), and (l)].

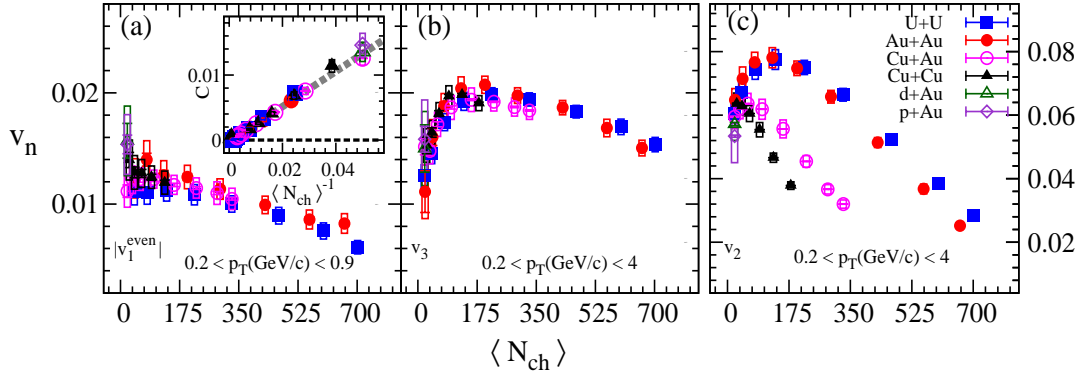


Fig. 29. Comparison of the $\langle N_{ch} \rangle$ dependence of v_1^{even} (a), v_3 (b) and v_2 (c) for all collision systems for the p_T selections indicated. The inset in (a) compares the extracted values of C vs. $\langle N_{ch} \rangle^{-1}$ for each system; the dashed line is drawn to guide the eye.

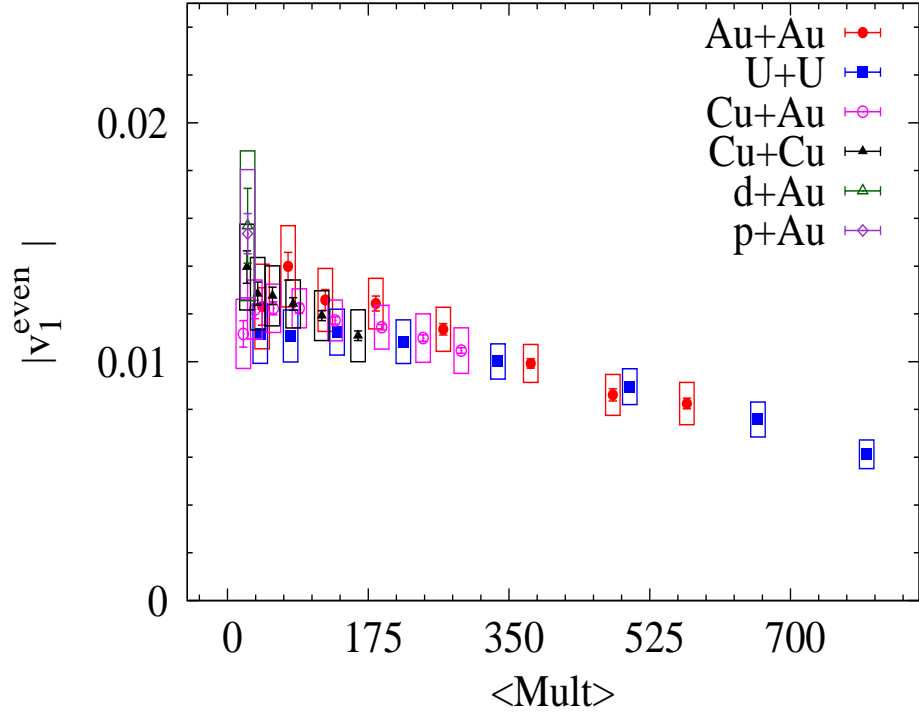


Fig. 30. The $\langle \text{Mult} \rangle$ dependence of v_1^{even} for all collision systems for the p_T selections indicated.

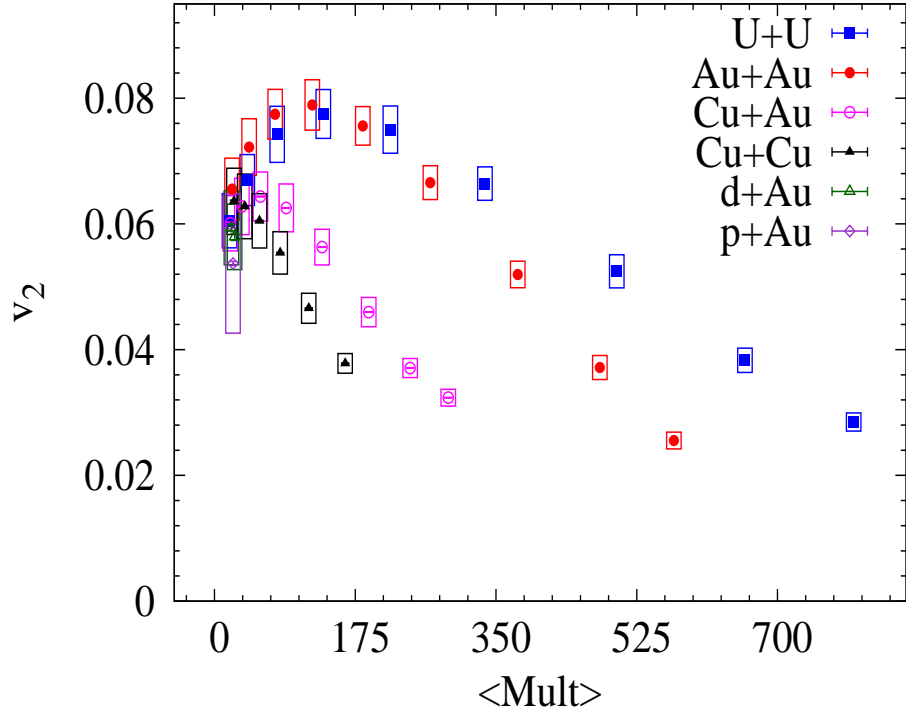


Fig. 31. The $\langle \text{Mult} \rangle$ dependence of v_2 for all collision systems for the p_T selections indicated.

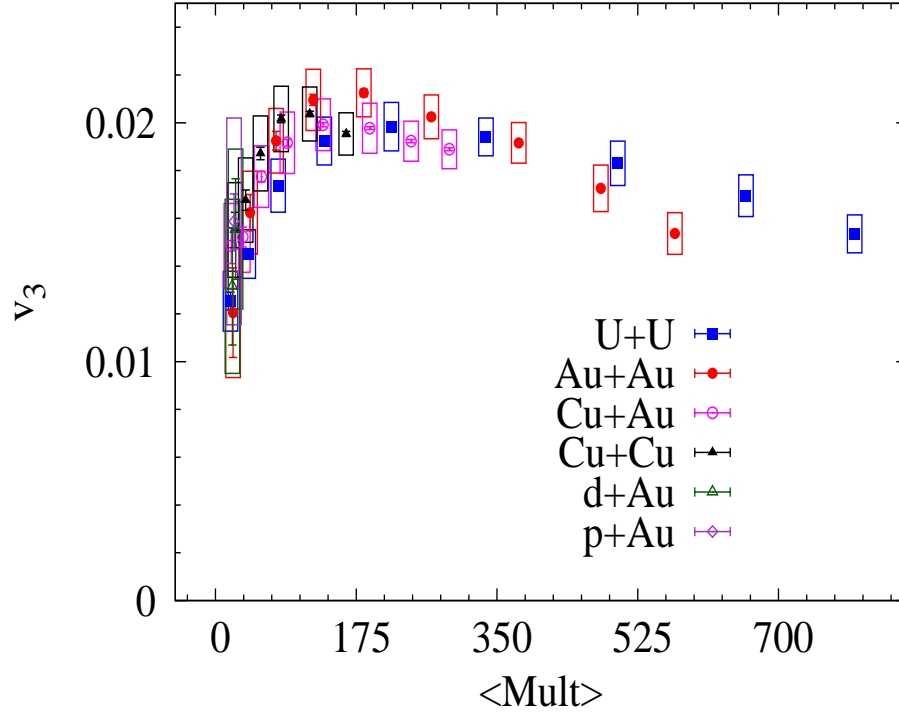


Fig. 32. The $\langle \text{Mult} \rangle$ dependence of v_3 for all collision systems for the p_T selections indicated.

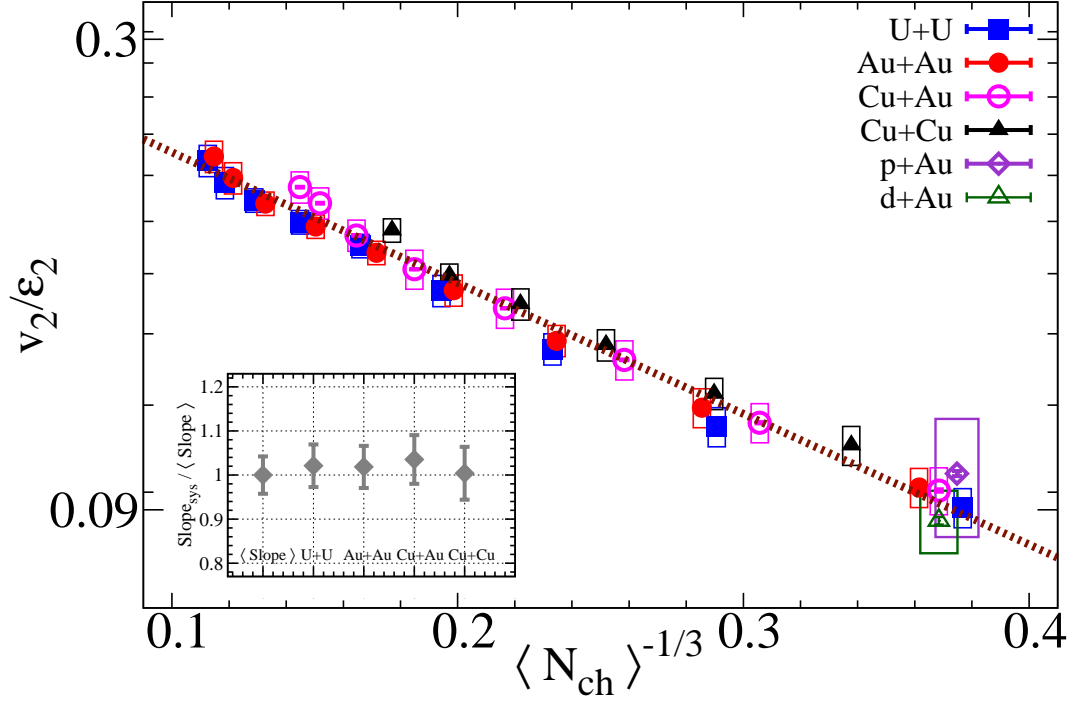


Fig. 33. $\ln(v_2/\varepsilon_2)$ vs. $\langle N_{\text{ch}} \rangle^{-1/3}$ for U+U, Au+Au, Cu+Au, Cu+Cu, d+Au and p+Au collisions as indicated. The v_2 data is the same as in Fig. 29(c). The curve represents a linear fit to the data. The inset shows the ratio of the slope extracted for each system over the slope extracted for the combined data sets.

Appendix A: Comparisons

Similar v_n measurements have been measured by Other collaborators. In this section, we compare with them measurements of v_2 . In Figs. 34, 35 and 36 we show that our v_2 is in good agreement with the other measurements.

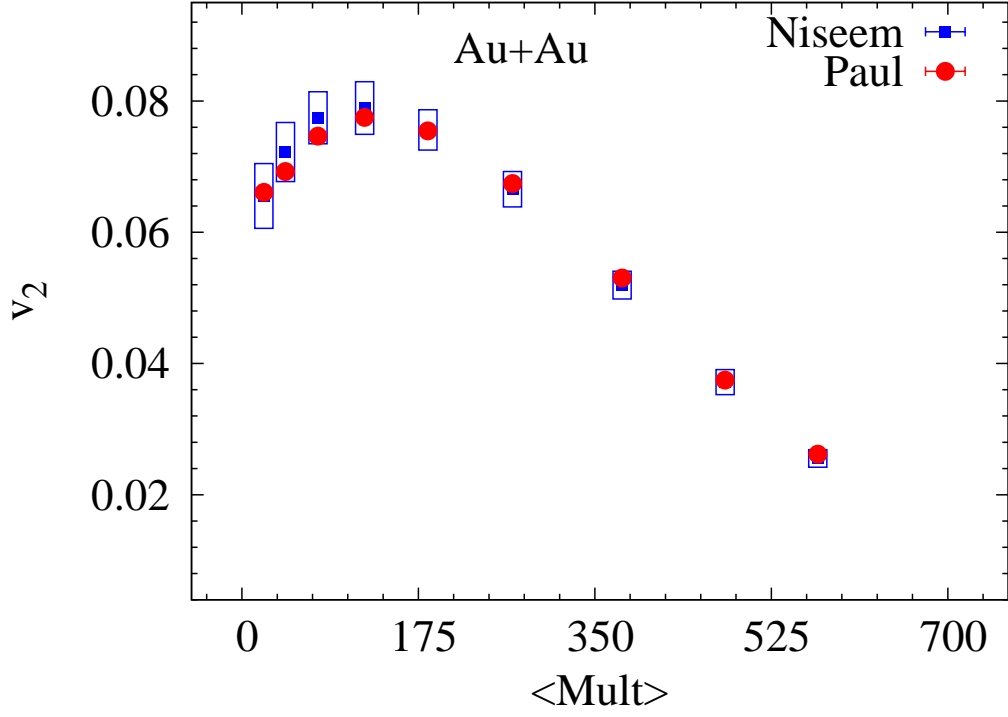


Fig. 34. The p_T -integrated v_2 vs $\langle \text{Mult} \rangle$ for $Au + Au$ at 200 GeV.

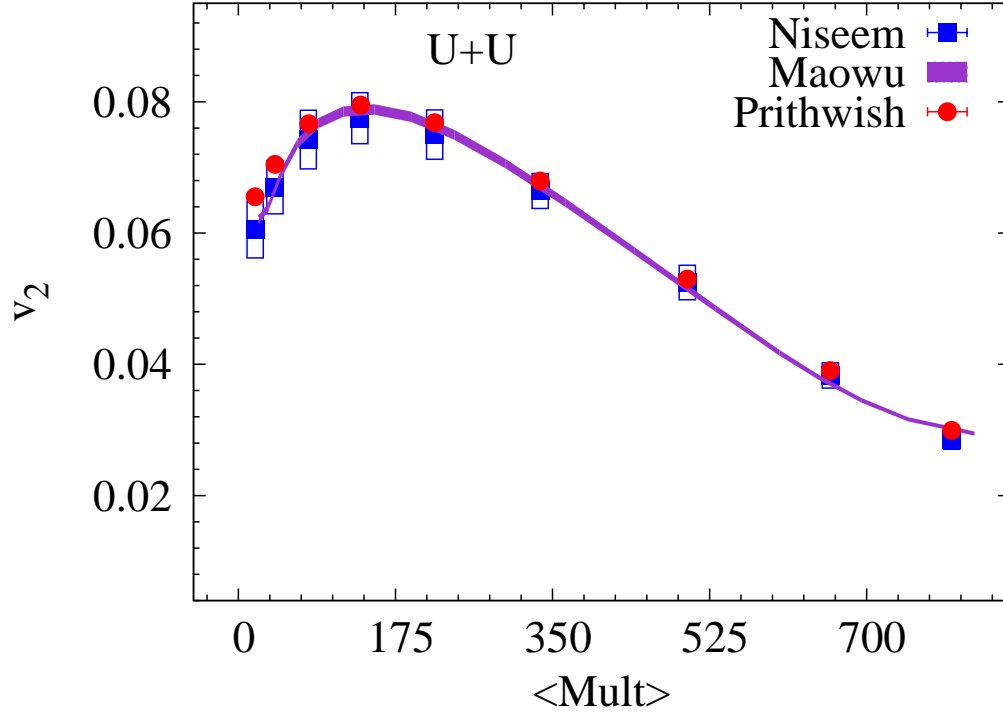


Fig. 35. The p_T -integrated v_2 vs $\langle Mult \rangle$ for $U + U$ at 139 GeV.

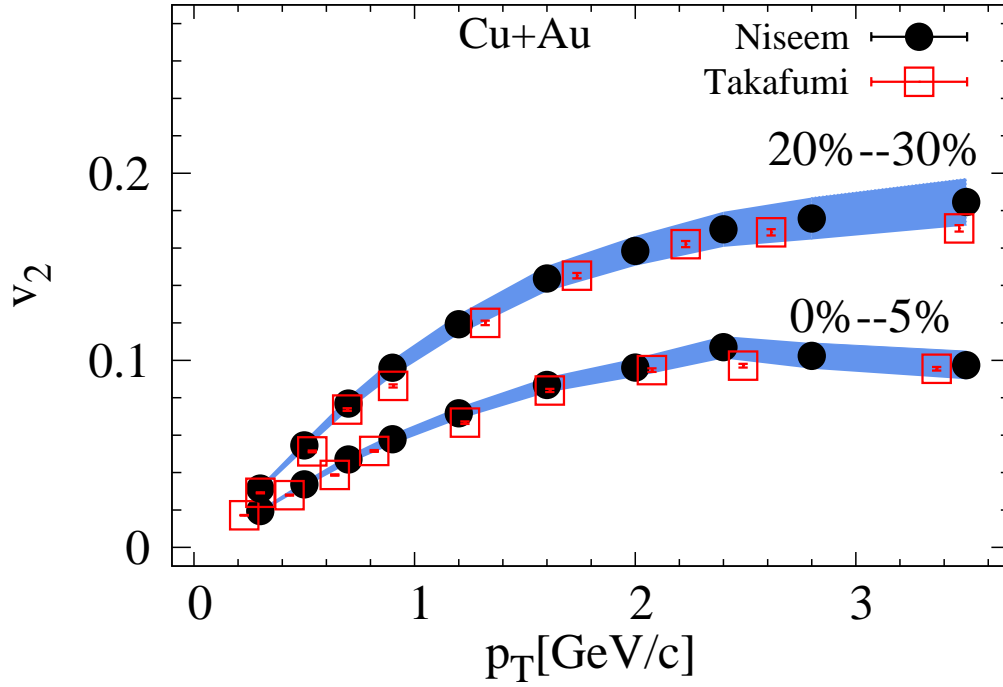


Fig. 36. The v_2 vs p_T for $Cu + Au$ at 200 GeV.

Appendix B: Multi-particle correlation

The multi-particle cumulant method is an important toll to study the nature of the azimuthal correlations observed in heavy-ion collisions. The second-order cumulant $c_2\{4\}$ are obtained after subtracting the correlations between two and four particles according to the following formula:

$$c_2\{4\} = \langle\langle 4 \rangle\rangle - 2\langle\langle 2 \rangle\rangle^2, \quad (\text{B1})$$

where $\langle\langle \rangle\rangle$ represent the averaging, performed first over particles in an event and then over all events within a given event class. In this work we had used the three sub event method [1701.03830] to study the $c_2\{4\}$ for defendant collision systems.

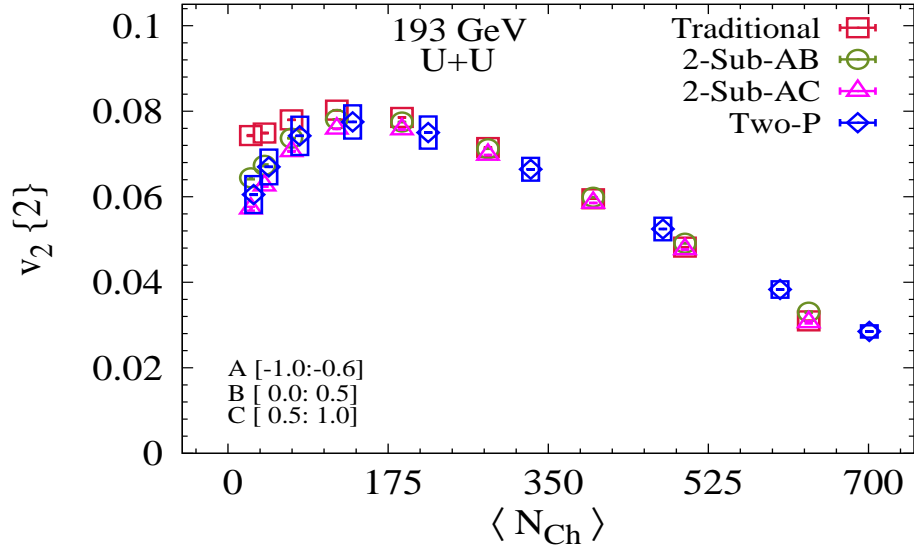


Fig. 37. Comparison between $v_2\{2\}$ using different method.

In Figs.37 and 38 we shows comparison between $v_2\{4\}$ using different method. The cumulant method give results that is in good agreement 2-particle correlation results and unfolding results.

??

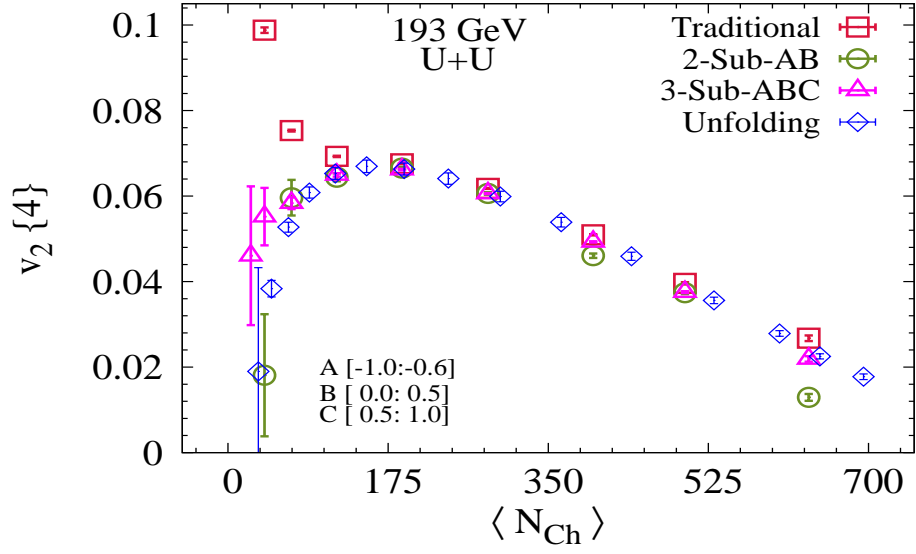


Fig. 38. Comparison between $v_2\{4\}$ using different method.

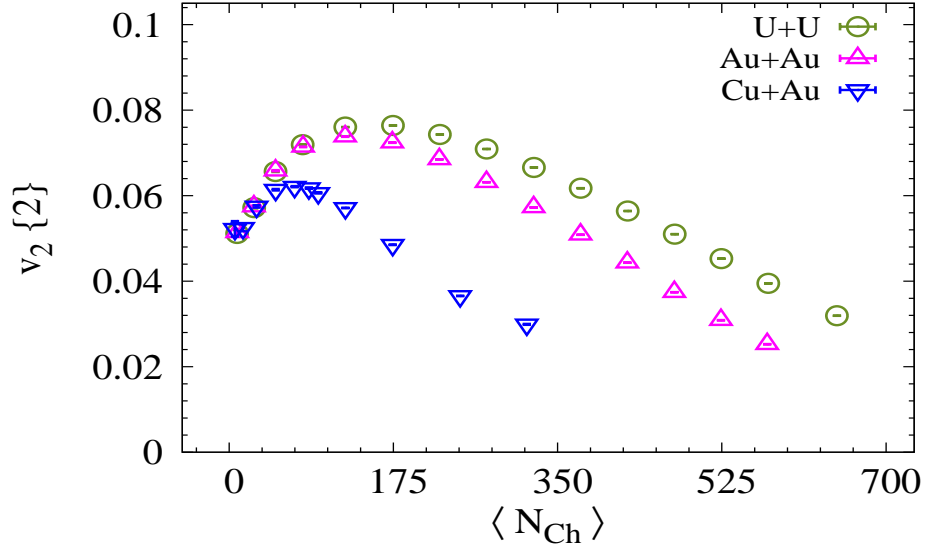


Fig. 39. Comparison of $v_2\{2\}$ for different systems.

Appendix C: The ϵ_2 used in this work

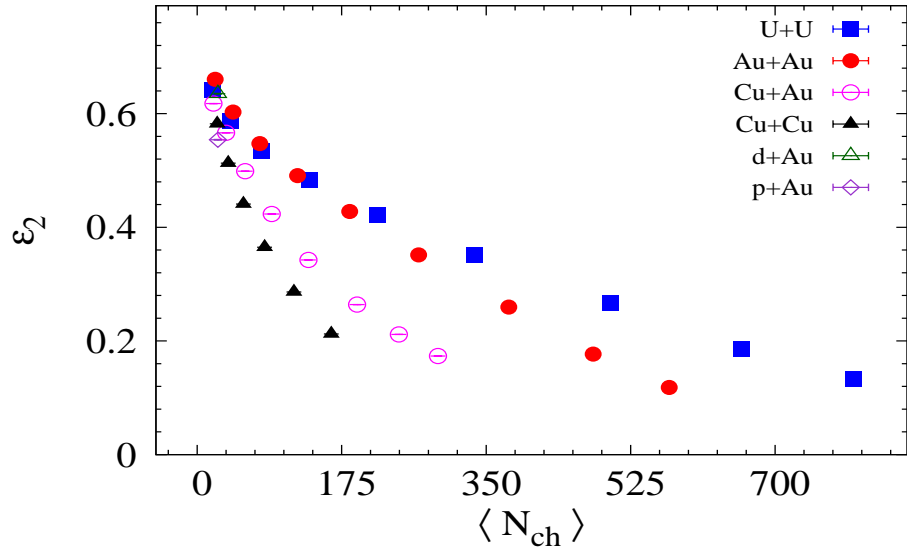


Fig. 40. The ϵ_2 used in this work using Quark Monte Carlo Glauber.